


Self-sustaining oscillation of two axonemal microtubules based on a stochastic bonding model between microtubules and dynein

T. Omori ^{1,*} S. Munakata,² and T. Ishikawa^{1,2}

¹*Department of Finemechanics, Tohoku University, Aramaki Aoba 6-6-01, Sendai, Miyagi Japan*

²*Department of Biomedical Engineering, Tohoku University, Aramaki Aoba 6-6-01, Sendai, Miyagi Japan*



(Received 3 March 2022; accepted 17 June 2022; published 7 July 2022)

The motility of cilia and flagella plays important physiological roles, and there has been a great deal of research on the mechanisms underlying the motility of molecular motors. Although recent molecular structural analyses have revealed the components of the ciliary axoneme, the mechanisms involved in the regulation of dynein activity are still unknown, and how multiple dyneins coordinate their movements remains unclear. In particular, the mode of binding for axonemal dynein has not been elucidated. In this study, we constructed a thermodynamic stochastic model of microtubule-dynein coupling and reproduced the experiments of Aoyama and Kamiya on the minimal component of axonemal microtubule-dynein. We then identified the binding mode of axonemal dynein and clarified the relationship between dynein activity distribution and axonemal movement. Based on our numerical results, the slip-bond mechanism agrees quantitatively with the experimental results in terms of amplitude, frequency, and propagation velocity, implying that axial microtubule-dynein coupling may follow a slip-bond mechanism. Moreover, the frequency and propagation velocity decayed in proportion to the fourth power of microtubule length, and the critical load of the trigger for the oscillation agreed well with Euler's critical load.

DOI: [10.1103/PhysRevE.106.014402](https://doi.org/10.1103/PhysRevE.106.014402)

I. INTRODUCTION

Cilia and flagella are motile cell organelles that have been conserved throughout evolution from ancient organisms, and play active roles in reproduction and development [1–3]. Fluid flow produced by ciliary and flagellar movements has been shown to play roles in airway clearance [4], left-right body asymmetry [2,3,5], and cell movements, such as those of spermatozoa [6,7]. The motility of cilia, which plays an important physiological role, is determined by the axonemal proteins within the cilia, and there has been a great deal of research on the mechanisms underlying the motility of molecular motors.

Recent molecular structural analyses have identified the components of the ciliary axoneme [8–10]. Typical eukaryotic cilia and flagella have nine doublet microtubules with a central pair of microtubules, the so-called “9+2” structure. The source of ciliary movement is the driving force of a molecular motor called dynein [8]. Dyneins are minus end-directed motors that use conformation-dependent changes associated with adenosine triphosphate (ATP) hydrolysis to attach to and walk along microtubules [8]. Axonemal dyneins are organized in two rows, the outer and inner dynein arms, which repeat periodically along with the doublet. The repeat unit is 96 nm in length in each doublet and the unit possesses four to seven dynein arms [10]. For the cilia as a whole to achieve bending motion, multiple dyneins must cooperate spatiotemporally, and it is thought that bending is achieved, for example, by a cross-sectional asymmetric distribution of dynein activity [9].

Several theoretical and computational studies have been conducted to clarify the mechanics of the ciliary or flagellar axoneme [11–15]. Brokaw [11] developed a sliding filament model, in which bending activation was controlled locally by the curvature of the flagellum. While Brokaw's model used the resistive force theory to describe fluid motion, Eloy and Lauga [13] adopted the more detailed hydrodynamic slender body theory to determine the energetically optimal ciliary waveform depending on the ciliary bending stiffness. Three-dimensional computational models have also been developed to describe the detailed three-dimensional structure of the nodal axonemes, and the relationship between the spatiotemporal distribution of the circumferential and longitudinal dynein activity and the ciliary waveform has been elucidated [12,15]. However, these previous theoretical models described dynein activity control as an artificially controlled boundary condition, and thus have not yet reproduced self-sustaining ciliary bending movements.

To clarify the mechanism of autonomous oscillation of cilia and flagella, various mathematical models have been proposed [11,16–29]. Camalet and Jülicher [18] expressed the internal active force density in the two-filament model by Fourier mode and introduced the perturbation parameter under linearized small-deformation, clarifying the critical perturbation parameter with self-organized beating via the Hopf bifurcation. They also showed that the wave propagation can be induced by dynamic instability, and the resulting patterns of motion do not depend on the microscopic mechanism of the instability but only the filament rigidity and hydrodynamic friction [19]. It has also been suggested that self-sustained oscillations may be caused by a steady active force rather than cyclic active stress [17,24]. Bayly and Dutcher [17] showed

*omori@tohoku.ac.jp

that a steady active force distributed in the axial direction led to dynamic structural instability and oscillation, called flutter motion. Collesano *et al.* [22] developed a two-clamp filament model driven by dynein motors and investigated the static geometry and active dynamics of the system. When the two filaments were equal in length, they observed a transition similar to Euler buckling, resulting in a planar shape. When the length ratio was further increased, they observed that after a second-order bifurcation, the system spontaneously took a nonplanar shape with broken chiral symmetry and transitioned back to a planar shape. Ling *et al.* [24] showed that two Hopf bifurcations exist under steady force, and a three-dimensional spinning oscillation and a two-dimensional planar beat can be formed. By analyzing the energy of the waves, Foster *et al.* [23] found that the torque generated by dynein is proportional to the microtubule sliding velocity. It has been suggested that the sliding friction of microtubules in the axoneme is much greater than the viscous resistance of the fluid surrounding the cilia. Mondal *et al.* [25] reported that the initiation of autonomous oscillations due to mechanical instability is due to relative strain-softening and shear-thinning caused by active stress acting on the microtubules. Han and Peskin [27] developed a three-dimensional axoneme model, which obeyed the geometric constraint of dyneins in circumferential and longitudinal directions. The dynein motors in their model were connected to each other through the structure of the cilia, and had an unstable symmetric steady state where the cilia were straight and all motors were under equal tension. It has been reported that the instability of this steady state leads to the emergence of globally stable limit cycle oscillations, which become ciliary motions. However, the above dynein regulation models are continuum-scale models and do not relate to dynein adhesion modes. Recent analytical studies [20,21,26,28,29] successfully reproduced asymmetric waveform of *Chlamydomonas* flagellum, synchronal beating of two adjacent flagella, etc. In these studies, flagellar motion was modeled by a coarse-grained two filaments representing two opposite microtubule pairs (pairs 3-4 and 8-9, for example). Flagellar beating was determined by a tug of war between two opposite internal active forces, and dynein activity was controlled by sliding velocity (or time derivative of curvature) rather than the curvature itself. Although these modeling reproduced experimental results, the timescale of dynein association and dissociation is about the flagellar beat frequency, and it is not yet possible to resolve adhesion and detachment at the molecular level. A gap still remains between the analysis of microscopic molecular movements and macroscopic flagellar movements.

Microscopically, microtubule-dynein adhesion has been analyzed by laser trapping [30–32] and fluorescence resonance energy transfer [33], and the binding dynamics are being elucidated at the molecular level. One of the theoretical models supporting these studies is the thermodynamic probability model proposed by Bell [34]. The Bell model represents protein-mediated adhesion as a stochastic process and, depending on the internal parameters, it is possible to describe qualitative differences in adhesion modes, such as slip bonds, which easily dissociate under strong external forces, and catch bonds, which become stronger under applied forces. For cytoplasmic dynein and microtubules,

tensile testing by laser trapping was carried out [31,32], and the results showed that dynein responded as a slip bond under forward tension [31]. However, another group reported that dynein has properties of catch bonds when subjected to high loads [32]. Nair *et al.* [35] theoretically developed a threshold force deformation model of cytoplasmic dynein motors, wherein catch bonding set in beyond a critical applied load force. They showed that catch bonding behavior manifests the mean transport velocity of a cellular cargo can increase with increase in opposing load force. Several sliding filament models of stochastic dynein movement have been developed theoretically [36–38]. Brokaw [11] has introduced a model of superadhesive elasticity between the attached dynein and the A-doublet, which allows movement perpendicular to the A-doublet, and developed a sliding filament model with adhesive forces that distort the attached dynein. This additional strain influenced the kinetics of dynein attachment and detachment. Similar to Aoyama and Kamiya’s experiments [39], the active slide was shown to operate only where bending propagation occurs from the base to the tip. Despite the model agrees the experimental results, the adhesion mechanism of dynein remains unresolved, since there have been different reports on the adhesion mode of cytoplasmic dynein [31–33,35,37,38], and there is no consensus regarding the binding dynamics of axonemal dynein.

Determination of the mode of adhesion of axonemal dynein may open up new avenues for dynein regulation. In particular, it is necessary to clarify the relationships among the distribution of dynein activity, the state of adhesion, and the mode of axonemal movement. Aoyama and Kamiya [39] examined the behavior of frayed axonemes of *Chlamydomonas*, and reported that a pair of doublet microtubules frequently displayed association and dissociation cycles in the presence of ATP. This experimental system is the smallest axonemal dynein-microtubule constituent unit, and the relationship between axonemal dynein binding and axonemal movement is expected to be clarified by reproducing the experiments of Aoyama and Kamiya [39]. In this study, we developed a numerical model of the dynein-microtubule adhesion mode based on the Bell model to reproduce the experiments of Aoyama and Kamiya [39]. We used this model to identify the adhesion mode of axonemal dynein and to elucidate the mechanical mechanism by which autonomous axonemal movement is achieved.

II. GOVERNING EQUATIONS AND NUMERICAL METHODS

A. Problem setting

To mimic the experiments of Aoyama and Kamiya [39], we considered a system with two doublet microtubules and dynein, and excluded other microtubule-modifying proteins (e.g., nexin, radial spokes) from the system. Two microtubules are located on an infinite plane wall at $z = 0$, as shown in Fig. 1(a). Nine doublet microtubules are assumed to be evenly distributed in the ciliary circumferential direction, and the two microtubules are placed at a distance of $\Delta x = \frac{2\pi \times a_{\text{cilium}}}{9} \simeq 70$ nm in the (x, z) plane, where $a_{\text{cilium}} (= 100$ nm [40]) is the radius of a cilium. The initial shape of the two microtubules

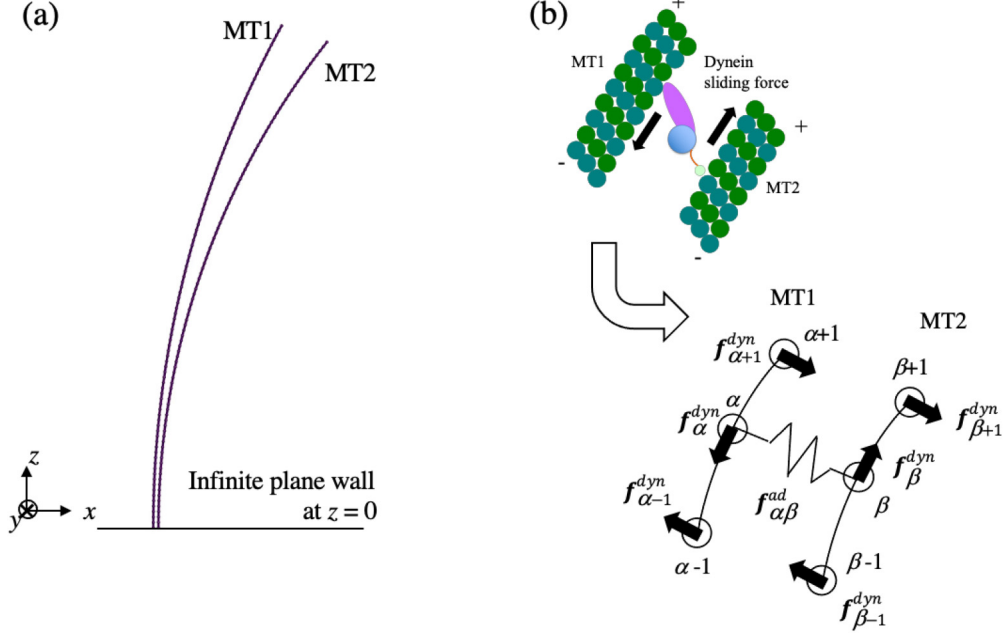


FIG. 1. Problem setting: (a) To mimic the experiment of Aoyama and Kamiya [39], two microtubules (MTs) are aligned in the (x, z) plane with the MT-MT distance of $\Delta x = 1.0 \times 10^{-2}L$ (~ 70 nm). Initial shapes of the MTs are taken from the image of Ref. [39], and the infinite plane wall is set at $z = 0$ using the Blakelet [42]. (b) Dynein sliding force is acting between the two MTs. Stochastic association and dissociation of the dynein head with microtubules is represented by the Bell model [34], and the sliding force and torque due to sliding friction of dynein are expressed as the combined force of tangential and normal forces on the nodes, which satisfies the force free conditions.

was taken from the image of Aoyama and Kamiya [39], and we assumed the reference shape corresponded to the initial shape.

A thermodynamic stochastic model was applied to determine the binding of dynein to microtubules and to describe the activation of dynein. When dynein-microtubule adhesion is determined to be on, the surface frictional forces associated with the walking of the dynein head are expressed as the sliding forces and torques acting between the two neighboring microtubules [cf. Fig. 1(b)].

The surrounding fluid is assumed to be an incompressible Newtonian fluid. Due to the small size of cilia (typically $10 \mu\text{m}$), the inertia effect of the fluid motion can be neglected. We then assume the flow is governed by the Stokes equation, which is described as a boundary integral equation. In the following sections, we present details of the governing equations and our numerical methodology.

B. Fluid mechanics

In eukaryotes, cilia have a slender structure with a radius of 100 nm compared to a length of 5 to $10 \mu\text{m}$ [40]. Doublet microtubules, which constitute the axoneme, have an even smaller radius of about 10 nm, and the flow field created by microtubules is described by the slender body theory [41]. The doublet microtubule is approximated by a curved rod and the arclength coordinate of the centerline is defined as $s \in (0, L)$, where L is the arclength of the microtubule. The flow field at point \mathbf{x} is located on the l th microtubule, $\mathbf{x}_l(s, t)$, is given

by [6,40]

$$\begin{aligned} \frac{\partial \mathbf{x}_l(s, t)}{\partial t} = & -\frac{1}{8\pi\mu} \boldsymbol{\Lambda}(s) \cdot \mathbf{f}(s) - \frac{1}{8\pi\mu} \int_{\text{self}} \\ & \times [\mathbf{J}(s, s') \cdot \mathbf{f}(s') + \mathbf{K}(s, s') \cdot \dot{\mathbf{f}}(s')] ds' \\ & - \frac{1}{8\pi\mu} \int_{\text{other}} [\mathbf{J}(s, s') + \mathbf{W}(s, s')] \cdot \mathbf{f}(s') ds', \end{aligned} \quad (1)$$

where \mathbf{f} is the force density per unit length. The first integral in the right-hand side of the equation is defined on l th microtubules, i.e., the self-term, and the last term is the velocity generated by other microtubules. \mathbf{J} is the Green's function including the Blakelet [42] to describe an infinite plane wall at $z = 0$, as given by

$$\begin{aligned} J_{ij}(s, s') = & J_{ij}^0(s, s') - J_{ij}^0(s, s^{\text{IM}}) + 2h^2 J_{ij}^D(s, s^{\text{IM}}) \\ & - 2h J_{ij}^{\text{SD}}(s, s^{\text{IM}}), \end{aligned} \quad (2)$$

where s^{IM} is a mirror image of the source point s' . J^0 is the free-space Green's function:

$$J_{ij}^0 = \frac{\delta_{ij}}{r} + \frac{r_i r_j}{r^3}, \quad (3)$$

J^D is the Green's function of a source doublet,

$$J_{ij}^D = (1 - 2\delta_{jz}) \left(\frac{\delta_{ij}}{R^3} - \frac{3R_i R_j}{R^5} \right), \quad (4)$$

J^{SD} is the Green's function of a Stokes doublet,

$$J_{ij}^{\text{SD}} = (1 - 2\delta_{ij}) \left(\frac{\delta_{ij}R_3 - \delta_{iz}R_j + \delta_{jz}R_i}{R^3} - \frac{3R_iR_jR_z}{R^5} \right), \quad (5)$$

$r = |\mathbf{r}|$, $\mathbf{r} = \mathbf{x}_l(s) - \mathbf{x}(s')$, $\mathbf{R} = \mathbf{x}_l - \mathbf{x}(s^{\text{IM}})$, and h is the height of the source point s' from the wall. $\mathbf{\Lambda}$ and \mathbf{K} are the local operators of the slender body theory, which are given by [41]

$$\Lambda_{ij}(s) = c[\delta_{ij} + t_i(s)t_j(s)] + 2[\delta_{ij} - t_i(s)t_j(s)], \quad (6)$$

and

$$K_{ij}(s, s') = -\frac{\delta_{ij} + t_i(s)t_j(s)}{|s - s'|}, \quad (7)$$

where $c = -\ln(\varepsilon^2 e)$, \mathbf{t} is the unit tangential vector to the centerline of each microtubule, $\varepsilon = a_{\text{MT}}/L$, and a_{MT} is the microtubule radius. We assume the length and radius of the microtubule are $L = 7 \mu\text{m}$ and $a_{\text{MT}} = 12.5 \text{ nm}$ [15], respectively, and the slenderness value ε is then set to $\varepsilon = 1.79 \times 10^{-3}$ in the present study. The slender body kernel \mathbf{W} is also given by [41]

$$W_{ij}(s, s') = \frac{(\varepsilon L)^2}{2} \left(\frac{\delta_{ij}}{r^3} - 3 \frac{r_i r_j}{r^5} \right). \quad (8)$$

C. Microtubule model

Next, we explain the solid mechanics of the microtubule model [43–45]. Each microtubule is assumed to be a thin curved rod, and the transverse shear stresses in the cross-section are neglected, i.e., the microtubule is modeled as an isotropic Eulerian rod. The microtubule is discretized at N nodes, and the elastic force at the α th node is described by a linear sum of the extensional and bending force:

$$\mathbf{F}_\alpha^e = \mathbf{F}_\alpha^{\text{ext}} + \mathbf{F}_\alpha^{\text{bend}}. \quad (9)$$

Note that the Greek indices represent the discrete node number, while the alphabetical indices, e.g., Eq. (2), represent the components of each tensor and vector. The extensional force \mathbf{F}^{ext} between the nodes α and β is given by

$$\mathbf{F}_\alpha^{\text{ext}} = k^{\text{ext}}(|\mathbf{r}_{\alpha\beta}| - r_{\alpha\beta}^0) \frac{\mathbf{r}_{\alpha\beta}}{|\mathbf{r}_{\alpha\beta}|}, \quad \mathbf{F}_\beta^{\text{ext}} = -\mathbf{F}_\alpha^{\text{ext}}, \quad (10)$$

where $\mathbf{r}_{\alpha\beta} = \mathbf{x}_\alpha - \mathbf{x}_\beta$, \mathbf{x}_α is the material point of the node α , $r_{\alpha\beta}^0$ is the reference length, and k^{ext} is the elastic coefficient. The bending force is also given by

$$\mathbf{F}_\alpha^{\text{bend}} = -k^{\text{bend}} \frac{\partial(\theta_\alpha - \theta_\alpha^0)}{\partial s} \mathbf{n}', \quad \mathbf{F}_{\alpha+1}^{\text{bend}} = \mathbf{F}_{\alpha-1}^{\text{bend}} = -\frac{1}{2} \mathbf{F}_\alpha^{\text{bend}}, \quad (11)$$

where k^{bend} is the bending coefficient, $\theta_\alpha = \cos(\mathbf{t}_{\alpha+1} \cdot \mathbf{t}_{\alpha-1})$, θ_α^0 is the reference angle. \mathbf{n}' is the s derivative of the normal vector and coincides with the tangent vector, where $|\mathbf{n}'| = 1$. The s -differential of θ is discretized by an unevenly spaced central differential:

$$\frac{\partial\theta_\alpha}{\partial s} \simeq \frac{\theta_{\alpha+1} - \theta_{\alpha-1}}{|\mathbf{x}_{\alpha+1} - \mathbf{x}_\alpha| + |\mathbf{x}_\alpha - \mathbf{x}_{\alpha-1}|}. \quad (12)$$

The bending coefficient k^{bend} is a coefficient that specifies the angular change of a discrete node, and does not correspond to the bending rigidity E_b in continuum mechanics. Quasi-static cantilever beam bending tests were carried out beforehand,

and the bending coefficient k^{bend} was adjusted so that the relationship between strain and distributed load was consistent with Hooke's law. When the number of nodes is $N = 98$ and the relationship between k^{bend} and E_b is set to $k^{\text{bend}}L/E_b = 45$, the error from the theoretical solution in continuum mechanics is less than 0.4%. We then decided to use the value of k^{bend} to $k^{\text{bend}}L/E_b = 45$. Once the elastic force \mathbf{F}_α^e is given, it is converted to force density by a central differential.

To keep the length of the microtubule constant, k^{ext} in Eq. (10) must be sufficiently large. With a large extensional force, the time step Δt must be sufficiently small to track the microtubule motion, and a large amount of computation time is required. Instead of using large k^{ext} , we applied the constraint of the forced displacement method as in previous studies [7,46]. The direction of the forced displacement is set to be tangential and the norm of the forced displacement is minimized by the Lagrange multiplier method [14,46]. Numerical iterations are carried out until the error of the length is less than a threshold value. In this case, the force in Eq. (10) contributes to acceleration of the iterative process. By applying the constraint, we confirmed that the change in length due to deformation was less than 1% with reasonable computational time.

D. Driving force generated by ATP hydrolysis of dynein

Morphological changes in dynein due to ATP hydrolysis and the surface frictional force are represented as the force acting on the adjacent microtubules when dynein-microtubule adhesion is determined to be on. As shown in Fig. 1(b), the dynein forces and torques are modeled as forces tangential and normal to the microtubule centerline, respectively [47]. Assuming dynein activation between nodes α and β of adjacent microtubules, the dynein force densities are expressed as follows [47]:

$$\mathbf{f}_\alpha^{\text{dyn}} = -\frac{F^{\text{dyn}}}{|\mathbf{x}_{\alpha+1} - \mathbf{x}_{\alpha-1}|} \mathbf{t}_\alpha, \quad \mathbf{f}_\beta^{\text{dyn}} = -\mathbf{f}_\alpha^{\text{dyn}}, \quad (13)$$

and

$$\mathbf{f}_{\alpha\pm 1}^{\text{dyn}} = \pm |\mathbf{f}_\alpha^{\text{dyn}}| \mathbf{n}_\alpha, \quad \mathbf{f}_{\beta\pm 1}^{\text{dyn}} = \pm |\mathbf{f}_\alpha^{\text{dyn}}| \mathbf{n}_\alpha, \quad (14)$$

where F^{dyn} is the force magnitude generated per dynein and \mathbf{n}_α is the unit normal vector. We treat F^{dyn} as a parameter while satisfying the force-free condition, as shown in Eqs. (13) and (14).

Recent laser trapping experiments measured the adhesive forces between dynein and microtubules [31], and a linear spring adhesive force was added to the model:

$$\mathbf{F}_\alpha^{\text{ad}} = G^{\text{ad}}(|\mathbf{r}_{\alpha\beta}| - r_0^{\text{dyn}}) \frac{\mathbf{r}_{\alpha\beta}}{|\mathbf{r}_{\alpha\beta}|}, \quad \mathbf{F}_\beta^{\text{ad}} = -\mathbf{F}_\alpha^{\text{ad}}, \quad (15)$$

where r_0^{dyn} is the natural length of the dynein, and G^{ad} is the adhesive constant.

E. Microtubule-dynein thermodynamic stochastic bonding model

To determine the adhesion and detachment of dynein, we used the Bell model [34] and Monte Carlo method. In the Bell model, the probabilities of adhesion and detachment for

a single dynein molecule at a given time step Δt are expressed as P_{on} and P_{off} , respectively:

$$P_{\text{on}} = 1.0 - \exp(-k_{\text{on}}\Delta t) \quad (16)$$

and

$$P_{\text{off}} = 1.0 - \exp(-k_{\text{off}}\Delta t). \quad (17)$$

The frequency of adhesion and detachment, k_{on} and k_{off} , are given by

$$k_{\text{on}} = k_{\text{on}}^0 \exp \frac{|\mathbf{F}_{\alpha}^{\text{ad}}|(\chi_{\beta} - \frac{1}{2}|\mathbf{r}_{\alpha\beta}|)}{k_b T} \quad (18)$$

and

$$k_{\text{off}} = k_{\text{off}}^0 \exp \frac{\chi_{\beta} |\mathbf{F}_{\alpha}^{\text{ad}}|}{k_b T}, \quad (19)$$

where k_{on}^0 and k_{off}^0 are coefficients that determine the frequency of adhesion and detachment, respectively, k_b is the Boltzmann constant, and T is the temperature. χ_{β} is reactive compliance, which determines the adhesion distance of dynein, and positive and negative χ_{β} can be used to describe qualitative differences between slip bonds, where the bond collapses when a large force is applied, and catch bonds, where the bond is strengthened by the force.

We assume that there are four outer dyneins in a periodic structure of 96 nm in the longitudinal direction of the microtubule [10]; assuming a microtubule length of $L = 7 \mu\text{m}$, each node represents three dynein bonds when the microtubule is discretized at 98 nodes. For each of the three dynein molecules at node α , a random number N_1 with $0 < N_1 < 1$ is given according to the Monte Carlo method, and if $P_{\text{on}} > N_1$, the number of adherent dynein molecules n_{α} is incremented. For adhered dynein molecules, a random number N_2 with $0 < N_2 < 1$ is given, and if $P_{\text{off}} > N_2$, the number of adhered dynein n_{α} is decremented. The number of bonding dynein n_{α} is changed in $0 \leq n_{\alpha} \leq 3$, and the sliding and adhesive forces are determined according to n_{α} . In the Bell model, the dynein kinetics are determined by the strain of microtubules, i.e., the distance between adjacent microtubules. For example, the probability of dissociation rate increases with the distance in the slip-bond mode. This mechanism is similar to the curvature (or sliding) control models proposed in some previous studies [16,18,48], and the Bell model is considered to be a type of geometric clutch model.

F. Numerical procedure

Initially, the two microtubules are located on the infinite plane wall with distance $\Delta x = 70 \text{ nm}$. The initial shape is taken from the image of Aoyama and Kamiya [39], and the reference shape is assumed to be the same as the initial shape. The effects of the reference shape are discussed in the Appendix. Each microtubule is discretized by $N = 98$ nodes. According to Eqs. (9), (10), and (11), the elastic force is computed in each time step. The adhesion between the microtubule and dynein is then determined using the Bell model and Monte Carlo method, and the dynein driving force is calculated according to n_{α} . Assuming force balance among elastic, driving, and fluid drag forces, the fluid drag force is expressed

TABLE I. Numerical constant used in the calculation.

Parameters	Value	Reference
Microtubule length L (μm)	7.0	[39,40]
Microtubule radius a_{MT} (nm)	12.5	[15]
Bending stiffness E_b ($\text{N}\cdot\text{m}^2$)	2×10^{-22}	[11,49]
Thermal energy $k_b T$ (J)	4.11×10^{-21}	
Natural length of dynein r_0^{dyn} (nm)	70	[31]
Adhesive constant G^{ad} ($\mu\text{N}\cdot\text{m}^{-1}$)	1	[31]
Dissociation frequency k_{off}^0 (s^{-1})	310	[33]
Adhesion frequency k_{on}^0 (s^{-1})	160	[33]

as the sum of the elastic and driving forces and is substituted into Eq. (1). To compute Eq. (1), we use a Gaussian numerical integration scheme as in our previous study [6,40]. Once the velocity is given, the nodal point \mathbf{x}_{α} is updated according to the no-slip boundary condition, $d\mathbf{x}_{\alpha}/dt = \mathbf{v}(\mathbf{x}_{\alpha})$, which is solved using a second-order Runge-Kutta method. The time step Δt is set to $\Delta t = 1.6 \times 10^{-7} \text{ s}$. We numerically confirmed the time convergence using a smaller Δt value; the results did not change markedly when using $\Delta t = 8.0 \times 10^{-8} \text{ s}$.

G. Parameter setting

Recent studies on the axoneme structure revealed coefficients related to axonemal molecules, such as the dynein driving force, binding frequency, and bending rigidity of microtubules. The results are summarized in Table I. The values of k_{on}^0 and k_{off}^0 are functions of ATP concentration, and are estimated to be 160 s^{-1} and 310 s^{-1} [33], respectively, under conditions of high ATP concentration. The effect of ATP concentration on the $k_{\text{on}}^0/k_{\text{off}}^0$ ratio is discussed in the Appendix. The remaining unknown quantity is χ_{β} , which determines the adhesion distance of dynein and is treated as an unknown parameter in this study. In the original Bell model, χ_{β} is considered to be related to the adhesion distance. In this study, we treat χ_{β} in the range of 10^{-10} to 10^{-7} meter. We also implement the mode change of slip bonds and catch bonds by positive and negative χ_{β} and analyze the microtubule motion in each mode.

To discuss the dynamics of microtubule motion, we introduced the sperm number (Sp) [13,14], a dimensionless number that expresses the ratio of viscous stress in oscillatory motions to bending elasticity, and is often used in situations dealing with sperm flagella and ciliary movements. The ratio of the unsteady viscous force to the bending elastic force in the motion of a thin rod can be expressed as Sp, which is useful for comparison with previous studies. In this study, Sp is defined as follows:

$$\text{Sp} = L(\mu k_{\text{off}}^0 / E_b)^{\frac{1}{4}}, \quad (20)$$

where L is the length of the microtubule, μ is the fluid viscosity, k_{off}^0 is the detachment frequency, and E_b is the bending stiffness. The effect of bending stiffness on Sp is $1/4$ power, whereas the length is proportional. Assuming that the viscosity of the surrounding fluid is in the range of 10^{-3} to 10^0 Pa s , the Sp estimated by the value in Table I is of the order

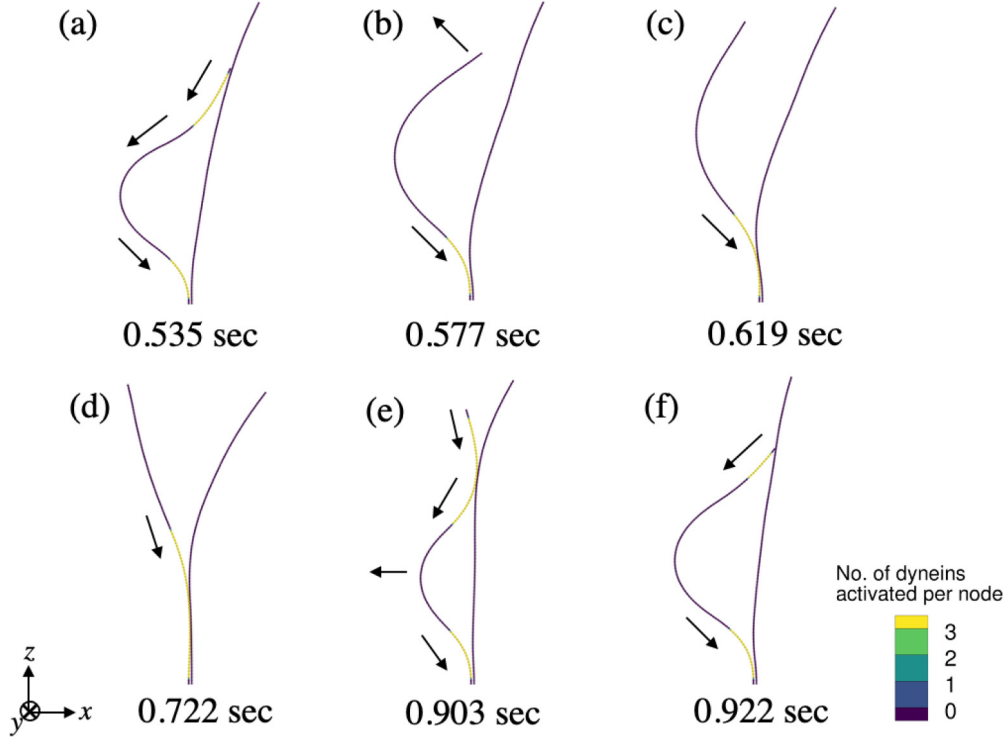


FIG. 2. Periodic oscillation of microtubules. The colors indicate the number of activated dyneins per computational node. Arrows are the motion of the left microtubule.

of 1 (about 1.4 to 7.8). In the present study, therefore, Sp is parameterized as 5.5 to 10.

III. RESULTS AND DISCUSSION

A. Self-sustaining oscillation of the axonemal microtubule

We first investigated the motions of the microtubules as slip bonds. The force generated by a single molecule of dynein was set to $F^{\text{dyn}} = 2$ pN, and the reactive compliance χ_β was set to 140 nm, respectively. Sp was also defined as $Sp = 7.8$.

Periodic oscillations were observed in the order of adhesion of dynein from the base of the microtubule, propagation of dynein activation to the tip of the microtubule, and divergence at the tip, as shown in Fig. 2. When the number of activated dynein molecules increased, the dynein sliding force acted as a compression force, causing the left microtubule, connected to the dynein tail, to buckle [cf. Fig. 2(e)]. After dissociation at the tip, the shape of the microtubule recovered to the reference shape via elastic force, and the activation occurred again at the root and the buckling repeated.

As shown in Eq. (15), a greater bond distance led to greater bonding force, but under slip bonds, a large bonding force caused a high probability of dissociation. Thus, a greater distance between the microtubules led to more dynein-microtubule dissociation, whereas the probability of bonding increased when they were closer to each other. This distance-controlled activation induced a stable periodic motion.

Self-sustaining oscillations of the microtubule were also observed in the experiment reported by Aoyama and Kamiya [39]. For more quantitative discussion, we next investigated the effects of the parameters χ_β and F^{dyn} on axoneme motion.

B. Three microtubule motions dependent on χ_β and F^{dyn}

We observed three microtubule motions with changes in χ_β and F^{dyn} : a quasistatic steady deformation mode [cf. Fig. 3(a)], an unstable mode with high-order buckling [cf. Fig. 3(b)], and a periodic oscillation mode. These mode changes under slip-bond conditions are summarized in Fig. 3(c). With large χ_β values, the microtubule showed steady deformation regardless of F^{dyn} . With slip bonds, higher values of χ_β increased the probability of dissociation and reduced the driving force acting on the microtubules. Conversely, under small χ_β values, the bonding probability increased and the compressive force acting on the microtubules became stronger, especially with large F^{dyn} values. The periodic oscillation mode occurred under intermediate values of both χ_β and F^{dyn} .

We observed the same three motions under catch-bond conditions (cf. Fig. 4). With catch bonds, large $|\chi_\beta|$ values increased the probability of dynein-microtubule bonding, often resulting in the unstable mode with high-order buckling. As in the case of slip bonds, the periodic oscillation mode was achieved only at appropriate χ_β and F^{dyn} values, whereas steady-state deformation was observed only under small F^{dyn} value. Although the stable oscillation region was smaller and less robust than that of slip bonds, the oscillation mode could be reproduced by catch bonds. Notably, when $\chi_\beta = 0$ (i.e., in the case of an ideal bond), the microtubules showed only steady deformation.

These results imply that oscillation can occur with both slip bonds and catch bonds. Thus, given the difficulty of identifying the adhesion mode between axonemal microtubules and dynein from the qualitative experimental results of the

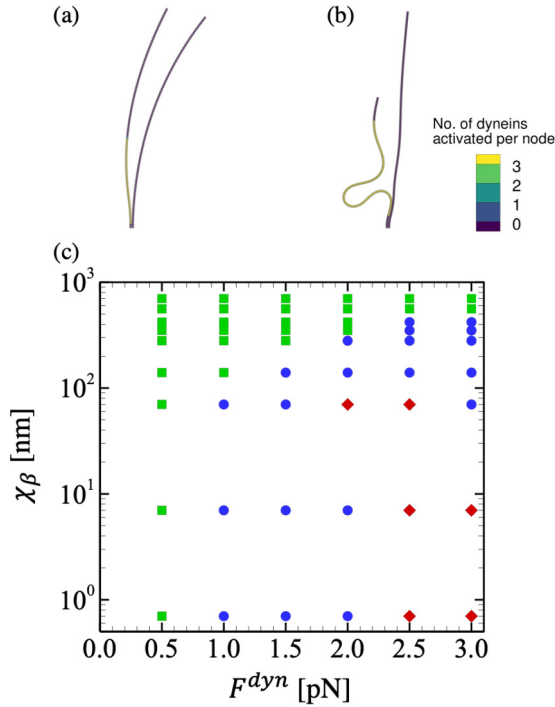


FIG. 3. Three different modes depending on the reactive compliance χ_β and dynein force F^{dyn} : (a) Steady deformation without oscillation, (b) unstable deformation with high-order buckling, and periodic oscillation modes as shown in Fig. 2. (c) Phase diagram of the slip-bond model in the parameter space of (χ_β, F^{dyn}) . Green square, blue circle, and red diamond indicate the steady deformation, periodic oscillation, and unsteady buckling modes, respectively.

oscillation mode, we next performed a quantitative comparison of the experimental results of adhesion distance and amplitude.

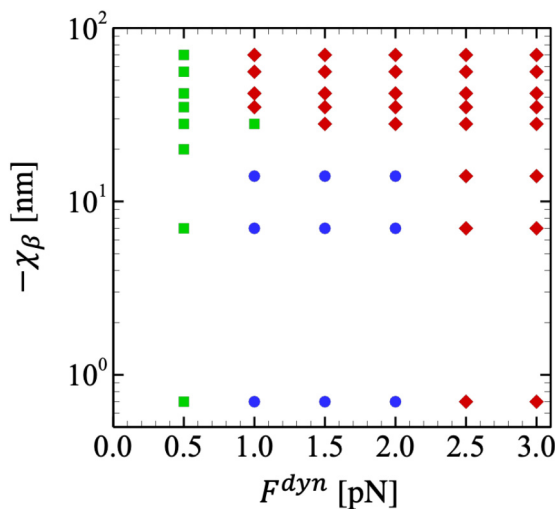


FIG. 4. Phase diagram of the catch-bond model. Green square, blue circle, and red diamond indicate the steady deformation, periodic oscillation, and unsteady buckling modes, respectively.

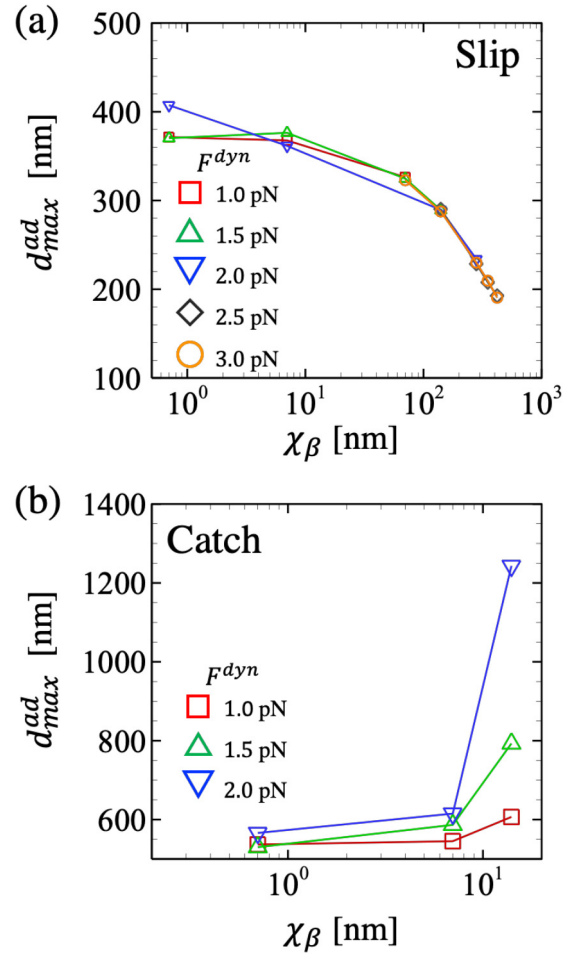


FIG. 5. Maximum adhesion distance with (a) the slip-bond and (b) the catch-bond.

C. Possible adhesion distance and amplitude under different bonding modes

For the oscillatory movements of axonemal microtubules observed in the former experiment, the amplitude was approximately $2 \mu\text{m}$ [39]. Here, we analyze the amplitudes and bonding distances obtained under slip-bond and catch-bond conditions.

The ensemble average of the bond distance at any given time t is defined as

$$d^{\text{ad}} = \frac{\sum_{\alpha}^N n_{\alpha} |\mathbf{r}_{\alpha\beta}|}{\sum_{\alpha}^N n_{\alpha}}. \quad (21)$$

We then take the maximum value of the average bond distance during computation to consider the possible bond distances for slip bonds and catch bonds. As shown in Fig. 5(a), for slip bonds, the maximum bonding distance was the same regardless of F^{dyn} . Its maximum value was about 400 nm and decreased monotonically with χ_β . This trend arose because a large χ_β value led to a high probability of dissociation.

For catch bonds, however, the maximum bonding distance increased with the magnitude of χ_β [cf. Fig. 5(b)]. For catch bonds, large $|\chi_\beta|$ values increased the probability of bonding and hence the adhesive bond strength. The high bond strength caused a backward loop in which the dissociation

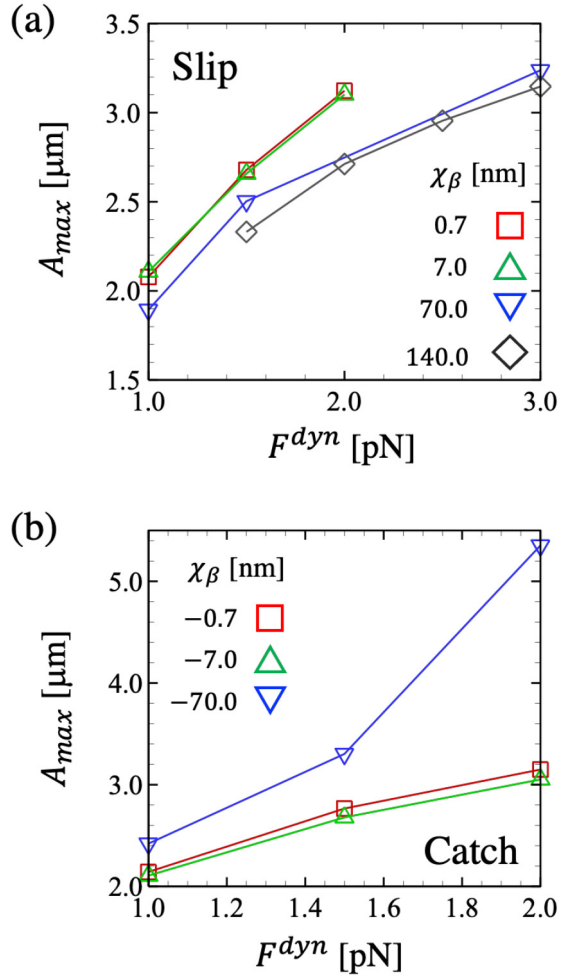


FIG. 6. Average amplitude of the oscillation mode with (a) the slip-bond and (b) the catch-bond.

frequency became increasingly smaller, so that the maximum bond distance exceeded $1 \mu\text{m}$ even in the oscillation mode. The maximum adhesion distance may be estimated to be a few times the dynein length (a few hundred nanometers at most), so micrometer adhesion distances are considered to be too large. In fact, no such long-distance adhesion was observed in the experiments.

We also investigated the amplitude of the oscillation, defined as the maximum distance between the microtubules; the spatiotemporal maximum amplitude is shown in Fig. 6. For both slip bonds and catch bonds, the maximum amplitude increased with the dynein force F^{dyn} . There was little difference in the effect of slip-bond and catch-bond conditions on the amplitude, and both models were in quantitative agreement with previous experimental results (around $2 \mu\text{m}$ [39]).

Both the slip-bond and catch-bond models reproduced oscillatory motion, but the slip-bond model had a large stable oscillatory region, whereas the catch-bond model had a relatively small region (cf. Figs. 3 and 4). In addition, the adhesive distance in the oscillation mode was larger for catch bonds. Based on the quantitative comparison of the adhesion distances and the robustness of the oscillation mode, axonal microtubule-dynein coupling likely follows a slip-bond

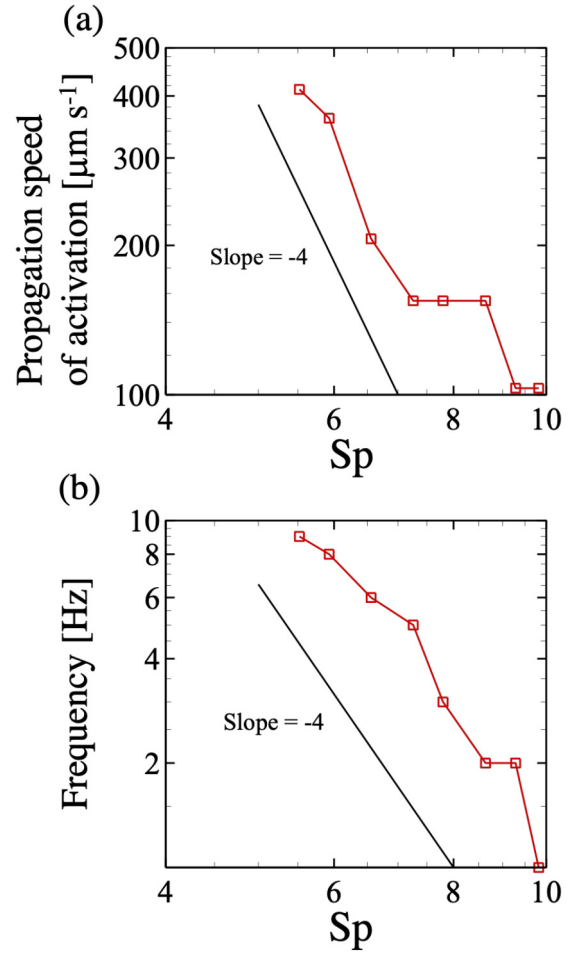


FIG. 7. Effect of the sperm number Sp on (a) the propagation speed and (b) the oscillation frequency.

mechanism. However, further quantitative comparison with experimental results is required before this can be determined conclusively.

D. Effect of sperm number on the oscillation dynamics

The previous sections focused on microtubule deformations and bond distances. Here, we consider time-varying dynamics. We first investigated the propagation speed of dynein activation from the root to the tip. χ_β and F^{dyn} were set to 140 nm and 2 pN , respectively. The results are summarized by Sp and are shown in Fig. 7(a). As Sp is a dimensionless number that is dependent on microtubule stiffness, length, fluid viscosity, and dissociation frequency, the results can be discussed for systems with different values of each. The propagation speed decayed approximately proportional to Sp^{-4} . As Sp is proportional to $1/4$ of the viscosity or dissociation frequency, this result indicates that the propagation velocity decreases inversely with these parameters, and likewise decays with the fourth power of microtubule length. The propagation velocity shown in the experiment of [39] was about $400 \mu\text{m/s}$, which confirmed the quantitative agreement of the propagation velocity with slip bonds (in the case of catch bonds, the propagation velocity was at most $280 \mu\text{m/s}$).

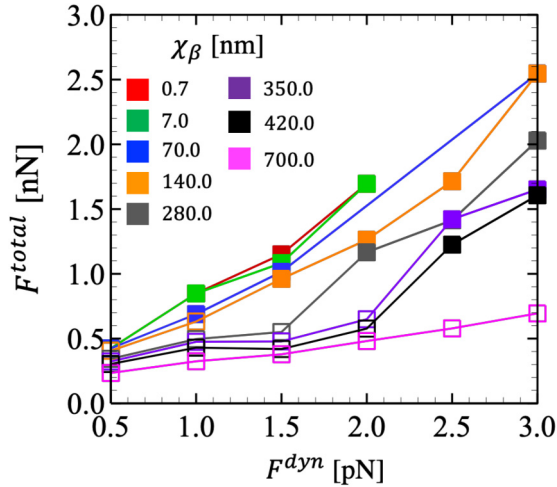


FIG. 8. Relationship between the total sliding force and the force produced by a single dynein head. Filled symbols indicate the oscillation mode, whereas the open symbol is the steady mode.

We then investigated the oscillation frequency with varying Sp . For the oscillation frequency, as well as for the propagation velocity, the decay was proportional to the fourth power of Sp [cf. Fig. 7(b)]. In a previous experiment, the frequency was about 9 Hz [39], in good agreement with the present results, where the frequency of the catch bond reached a maximum of about 4 Hz. Using the slip-bond model, the experimental results can be quantitatively reproduced both in terms of deformation and dynamic motion. In addition, these results imply that the most important parameter describing microtubule dynamics is microtubule length, and that, given the same driving force, the velocity of motion decays in proportion to the fourth power of the length.

E. Force required for the oscillation mode

When two doublet microtubules are associated for a certain length, dynein generates sliding force, resulting in a large bending moment at the base. For homogeneous and isotropic straight rods, Euler's critical load, the load that causes the column to buckle and fail, is given by

$$F^{\text{Euler}} = \pi^2 E_b / L^2. \quad (22)$$

Then, the force required to bend over a length of $1 \mu\text{m}$ may be about 2 nN. To compare the critical load in this simulation with the Eulerian load, the total sliding force acting on the microtubule is determined using the following equation:

$$F^{\text{total}} = \max_{t \in T} \sum n_{\alpha}(t) F^{\text{dyn}}, \quad (23)$$

where T is the period.

The total force for slip bonds is shown in Figure 8. Regardless of the value of χ_{β} , when F^{total} exceeded 1 nN, buckling dissociation occurred at the root under all conditions and the periodic oscillation mode was observed. This result is quantitatively in agreement with the Eulerian critical load, indicating that the oscillation mode is triggered by root buckling due to compressive loading.

Aoyama and Kamiya [39] also discussed the critical load for root buckling. They estimated that a compressive force of 2.3 nN was required for the bend, which would require 400 to 2000 dynein heads over a length of 2 to $10 \mu\text{m}$. Our results support their buckling model and provide a theory for self-sustaining oscillatory motion in two-microtubule systems.

IV. CONCLUSION

In this study, we developed a model for stochastic bonding between microtubules and dynein, and simulated the motion of two axonemal microtubules, mimicking the experiment of Aoyama and Kamiya [39].

Both slip-bond and catch-bond models reproduced the oscillation mode; however, the slip-bond model was in quantitative agreement with the experimental results in terms of amplitude, frequency, and propagation velocity, implying that axial microtubule-dynein coupling may follow a slip-bond mechanism. Moreover, the frequency and propagation velocity decayed in proportion to the fourth power of the microtubule length, and the critical load of the trigger for the oscillation mode agreed well with Euler's critical load. These results provide a theoretical understanding of the previously reported microtubule vibration and help to clarify the as-yet undetermined mechanism of dynein activity regulation.

ACKNOWLEDGMENTS

The authors acknowledge the support of JSPS KAKENHI (Grants No. 18K18354, No. 21H04999, and No. 21H05308) and JST PRESTO (Grant No. JPMJPR2142).

T.O. and T.I. designed research; T.O. and S.M. performed simulation; T.O., S.M., and T.I. analyzed data; T.O., S.M., and T.I. wrote the paper.

APPENDIX

1. Effect of microtubule reference shape

Here, we show the effect of the microtubule reference shape. In the main text, the reference shape was set as curved, which corresponds to the initial shape. The effect of the reference shape on the motion was investigated by calculating the case where the reference shape was a straight line while keeping the initial shape. The oscillation mode was also observed when the reference shape was changed to straight. Table II shows a comparison of the results for the slip-bond model, $F^{\text{dyn}} = 2 \text{ pN}$, $\chi_{\beta} = 140 \text{ nm}$, $Sp = 7.8$, $k_{\text{on}}^0/k_{\text{off}}^0 = 0.516$. There were no marked changes in most of the analyses, implying that motion was not highly dependent on the reference geometry.

TABLE II. Effect of the reference shape: Curved rod versus straight rod.

Parameters	Curve	Straight
Max amplitude A_{max} (μm)	2.7	2.52
Possible adhesive distance $d_{\text{max}}^{\text{ad}}$ (nm)	289	286
Total sliding force F^{total} (nN)	1.26	1.37
Propagation velocity ($\mu\text{m s}^{-1}$)	154.6	154.6
Oscillation frequency (Hz)	3	3

2. Effect of ATP concentration

In this study, the frequencies of adhesion and detachment k_{on}^0 and k_{off}^0 were defined as variables dependent on ATP concentration, as described in Sec. II. Imamura *et al.* [33] demonstrated the response of dynein attachment and detachment frequency to varying ATP concentration via fluorescence resonance energy transfer. The adhesion frequency was almost constant regardless of the ATP concentration, whereas the detachment frequency showed a rapid decay at low concentrations. Aoyama and Kamiya [39] also reported that microtubules showed almost stationary adhesion mode under conditions of low ATP, and it is possible that the change in adhesion dynamics by the change of ATP concentration leads to a change in macroscopic microtubule motion. In the main text, a high ATP concentration was assumed and the

$k_{\text{on}}^0/k_{\text{off}}^0$ ratio was set to 0.516. Here, a low ATP concentration is assumed and the ratio was reset to $k_{\text{on}}^0/k_{\text{off}}^0 = 10$ to examine the effect of ATP concentration. With the parameters of $F^{\text{dyn}} = 2$ pN, $\chi_{\beta} = 140$ nm (slip-bond model), no mode change from oscillatory to steady-state adhesion was observed even when the detachment frequency was changed by a factor of 20. Conversely, mode change could be achieved by F^{dyn} and χ_{β} , as shown in Fig. 3. F^{dyn} and χ_{β} control the probability as exponential functions, whereas k_{on}^0 and k_{off}^0 affect it as coefficients of the exponential function. These results indicate that the sensitivity of F^{dyn} and χ_{β} to ATP is more important than the attachment and detachment frequency. A decrease in ATP concentration may lead to an increase in χ_{β} or a decrease in F^{dyn} . Further investigations are therefore required.

-
- [1] R. E. Goldstein, *Annu. Rev. Fluid Mech.* **47**, 343 (2015).
- [2] S. Nonaka, Y. Tanaka, Y. Okada, S. Takeda, A. Harada, Y. Kanai, M. Kido, and N. Hirokawa, *Cell* **95**, 829 (1998).
- [3] K. Shinohara, A. Kawasumi, A. Takamatsu, S. Yoshida, Y. Botilde, N. Motoyama, W. Reith, B. Durand, H. Shiratori, and H. Hamada, *Nat. Commun.* **3**, 622 (2012).
- [4] K. Kikuchi, T. Haga, K. Numayama-Tsuruta, H. Ueno, and T. Ishikawa, *Annu. Biomed. Eng.* **45**, 1048 (2017).
- [5] N. Hirokawa, Y. Okada, and Y. Tanaka, *Annu. Rev. Fluid Mech.* **41**, 53 (2009).
- [6] T. Omori and T. Ishikawa, *Phys. Rev. E* **93**, 032402 (2016).
- [7] N. Taketoshi, T. Omori, and T. Ishikawa, *Phys. Fluids* **32**, 101901 (2020).
- [8] J. Lin, K. Okada, M. Raytchev, M. C. Smith, and D. Nicastro, *Nat. Cell Biol.* **16**, 479 (2014).
- [9] J. Lin and D. Nicastro, *Science* **360**, eaar1968 (2018).
- [10] H. Ueno, T. Ishikawa, K. H. Bui, K. Gonda, T. Ishikawa, and T. Yamaguchi, *Nanomedicine* **8**, 1081 (2012).
- [11] C. J. Brokaw, *Biophys. J.* **12**, 564 (1972).
- [12] D. Chen, D. Norris, and Y. Ventikos, *Med. Eng. Phys.* **33**, 857 (2011).
- [13] C. Eloy and E. Lauga, *Phys. Rev. Lett.* **109**, 038101 (2012).
- [14] H. Gadelha, E. A. Gaffney, D. J. Smith, and J. C. Kirkman-BrownIshi, *J. R. Soc. Interface* **7**, 1689 (2010).
- [15] T. Omori, H. Sugai, Y. Imai, and T. Ishikawa, *J. Biomech.* **61**, 242 (2017).
- [16] C. J. Brokaw, *Proc. Natl. Acad. Sci. USA* **72**, 3102 (1975).
- [17] P. V. Bayly and S. K. Dutcher, *J. R. Soc. Interface* **13**, 20160523 (2016).
- [18] S. Camalet and F. Julicher, *New J. Phys.* **2**, 324 (2000).
- [19] S. Camalet, F. Julicher, and J. Prost, *Phys. Rev. Lett.* **82**, 1590 (1999).
- [20] B. Chakrabarti and D. Saintillan, *Phys. Rev. Fluids* **4**, 043102 (2019).
- [21] B. Chakrabarti and D. Saintillan, *Phys. Rev. Lett.* **123**, 208101 (2019).
- [22] L. Collesano, I. Guido, R. Golestanian, and A. Vilfan, *J. R. Soc. Interface* **19**, 20210693 (2022).
- [23] K. W. Foster, J. Vidyadharan, and A. S. Sangani, *Cytoskeleton* **74**, 260 (2017).
- [24] F. Ling, H. Guo, and E. Kanso, *J. R. Soc. Interface* **15**, 20180594 (2018).
- [25] D. Mondal, R. Adhikari, and P. Sharma, *Sci. Adv.* **6**, eabb0503 (2020).
- [26] D. Oriola, H. Gadelha, and J. Casademunt, *R. Soc. Open Sci.* **4**, 160698 (2017).
- [27] J. Han and C. S. Peskin, *Proc. Natl. Acad. Sci. USA* **115**, 4417 (2018).
- [28] I. H. Riedel-Kruse, A. Hilfinger, J. Howard, and F. Julicher, *HFSP J.* **1**, 192 (2007).
- [29] P. Sartori, V. F. Geyer, A. Scholich, F. Julicher, and J. Howard, *eLife* **5**, e13258 (2016).
- [30] R. Mallik, A. K. Rai, P. Barak, A. Rai, and A. Kunwar, *Trends Cell Biol.* **23**, 575 (2013).
- [31] M. P. Nicholas, F. Berger, L. Rao, S. Brenner, C. Cho, and A. Gennerich, *Proc. Natl. Acad. Sci. USA* **112**, 6371 (2015).
- [32] A. K. Rai, A. Rai, A. J. Ramaiya, R. Jha, and R. Mallik, *Cell* **152**, 172 (2013).
- [33] K. Imamura, T. Kon, R. Ohkura, and K. Sutoh, *Proc. Natl. Acad. Sci. USA* **104**, 16134 (2007).
- [34] G. I. Bell, *Science* **200**, 618 (1978).
- [35] A. Nair, S. Chandel, M. K. Mitra, S. Muhuri, and A. Chaudhuri, *Phys. Rev. E* **94**, 032403 (2016).
- [36] C. J. Brokaw, *Cytoskeleton* **71**, 273 (2014).
- [37] A. Kunwar, S. K. Tripathy, J. Xu, and S. P. Gross, *Proc. Natl. Acad. Sci. USA* **108**, 18960 (2011).
- [38] H. P. Singh, A. Takshak, U. Mall, and A. Kunwar, *Int. J. Mod. Phys. C* **27**, 1650137 (2016).
- [39] S. Aoyama and R. Kamiya, *Biophys. J.* **89**, 3261 (2005).
- [40] H. Ito, T. Omori, and T. Ishikawa, *J. Fluid Mech.* **874**, 774 (2019).
- [41] A.-K. Tornberg and M. J. Shelly, *J. Comput. Phys.* **196**, 8 (2004).
- [42] J. R. Blake, *Proc. Cambridge Philos. Soc.* **70**, 303 (1971).
- [43] J. Elgeti and G. Gompper, *Proc. Natl. Acad. Sci. USA* **110**, 4470 (2013).

- [44] L. D. Landau and E. M. Lifshitz, *Theory of Elasticity*, 3rd ed. (Butterworth-Heinemann, Oxford, UK, 2009).
- [45] S. D. Olson, S. S. Suarez, and L. J. Fauci, *J. Theor. Biol.* **283**, 203 (2011).
- [46] J. B. Freund, *Phys. Fluids* **19**, 023301 (2007).
- [47] T. Omori, M. Lu, and T. Ishikawa, *J. Biomech. Sci. Eng.* **13**, 17-00467 (2018).
- [48] Y. Morita and C. Shingyoji, *Curr. Biol.* **14**, 2113 (2004).
- [49] M. J. Shelly, *Annu. Rev. Fluid Mech.* **48**, 487 (2016).